Microresonator Dissipative Kerr Solitons Synchronized to an Optoelectronic Oscillator

Wenle Weng, Jijun He, Aleksandra Kaszubowska-Anandarajah, Prince M. Anandarajah, and Tobias J. Kippenberg

Phys. Rev. Applied **17**, 024030 — Published 10 February 2022

DOI: 10.1103/PhysRevApplied.17.024030

Microresonator Dissipative Kerr Solitons Synchronized to an Optoelectronic Oscillator

Wenle Weng,[1, 2, *] Jijun He,[1] Aleksandra Kaszubowska-Anandarajah,[3]
Prince M. Anandarajah,[4, †] and Tobias J. Kippenberg[1, ‡]

[1] *Institute of Physics, Swiss Federal Institute of Technology Lausanne (EPFL), CH-1015 Lausanne, Switzerland*
[2] *Institute for Photonics and Advanced Sensing (IPAS), and School of Physical Sciences, The University of Adelaide, Adelaide, South Australia 5005, Australia*
[3] *CONNECT Research Centre, Dunlop Oriel House, Trinity College Dublin, Dublin 2, Ireland*
[4] *Photonics Systems and Sensing Laboratory, School of Electronic Engineering, Dublin City University, Glasnevin D 9, Ireland*

Using phase-modulation-induced potential gradient whose period is synchronized to a microwave optoelectronic oscillator, dissipative Kerr solitons generated in a crystalline optical microresonator are trapped by the soliton tweezing effect, exhibiting a stabilized soliton repetition rate. In the meantime, side-mode suppression of the microwave signal is enabled by the photodetection of the soliton train. Substantiated both experimentally and theoretically, the hybrid system produces a drift-reduced microcomb and a spectrum-purified optoelectronic oscillator simultaneously, yielding a low-cost toolkit for microwave and optical metrology.

I. INTRODUCTION

Formed from the double balance of cavity loss and external pump on the one hand, and cavity dispersion and Kerr nonlinearity on the other, dissipative Kerr solitons (DKSs) are spatiotemporally localized lightwave structures that give rise to microresonator optical frequency combs (microcombs) [1]. In the past few years, the studies on microresonator DKSs have seen a remarkable proliferation into a wide variety of applications, including spectroscopy [2, 3], ranging [4, 5], time-keeping [6], and parallel photonic processing [7, 8]. While in many applications feedback control is implemented to stabilize the repetition rate of DKS, an alternative approach of using periodic pumping waveform to synchronize the DKS has achieved considerable frequency drift suppression, leading to the successful demonstrations of astrospectrometer calibration [9], deterministic single-soliton state initiation [10, 11], and nonlinear filtering of radiofrequency (rf) signals [12–14]. Yet, a microwave synthesizer of high performance is indispensable for producing the periodic pumping fields in these prior works, which substantially increases the system cost and footprint.

Based on a delayed positive feedback loop, an optoelectronic oscillator (OEO) is a simple and inexpensive device that can generate stable microwave signals [15, 16]. Since the quality factor (Q) of the feedback loop can be easily enhanced by increasing the length of the low-loss optical delay line, optical fibers with a length of a few to a few tens of kilometers are frequently adopted to develop OEOs with ultralow frequency drifts and phase noise [17–20]. Despite the obvious benefit, a serious issue of side-mode oscillation is triggered by the long fiber delay line at the same time. As the free spectral range (FSR) of the long OEO loop is very small in comparison with the bandwidth of the rf-frequency-selective filter, a large number of an OEO's resonances can exist within the oscillation bandwidth. As a result, multiple intensive side-mode oscillations are excited together with the main OEO oscillation at the offset frequencies of the loop FSR and its harmonics, leading to unwanted spikes and elevated noise level in the phase noise spectrum. To cope with this issue, advanced methods including using Vernier effect with a multiloop configuration [21] and exploiting the phenomenon of parity-time-symmetry breaking with coupled modes [22, 23] have been proposed and experimentally verified, showing high side-mode suppression ratios. Yet, these approaches require significantly increased structural complexity, which may severely limit their stable operation in practical scenarios.

In this work, by utilizing a bias-current-modulated semiconductor gain-switched laser (GSL) [11, 24] as the optical source, we develop an OEO to produce a stable microwave frequency that is close to the repetition rate of the DKSs generated in a crystalline microresonator. Using this self-started microwave signal as the rf source for pump laser modulation, we create intracavity phase gradient as a soliton tweezer to trap DKSs [12], thus synchronizing the DKS repetition rate to the OEO frequency. Our experiment shows that such a synchronization allows for the reduction of the soliton repetition rate drift by up to two orders of magnitude. In addition, the photodetection of the synchronized DKSs reproduces the OEO frequency with a purified phase noise at offset frequencies above 7 kHz. In particular, the intensive side-mode oscillations of the OEO are suppressed by at least 17 dB. To corroborate the experimental observations, extensive modelling of the OEO and numerical simulation of DKS dynamics are performed, showing that the trapped DKSs may be applied as side-mode suppressors for different types of OEOs.

* wenle.weng@adelaide.edu.au
† prince.anandarajah@dcu.ie
‡ tobias.kippenberg@epfl.ch

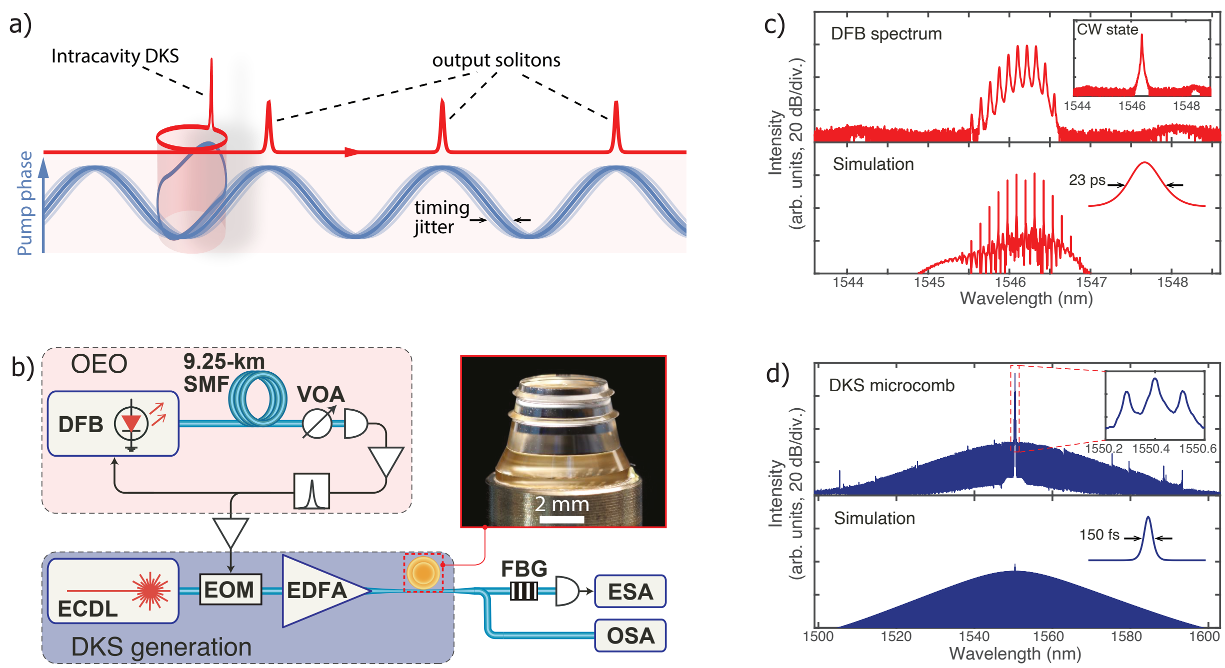

Figure 1. Using the phase gradient of a pump laser to synchronize microresonator DKSs to a GSL-based OEO. (a) The principle of DKS trapping. (b) Schematic of the experimental setup. A picture of the MgF_2 microresonator is displayed too. SMF: single-mode fiber; VOA: variable optical attenuator; EDFA: erbium-doped fiber amplifier; FBG: fiber Bragg grating notch filter. (c) The upper panel shows the optical spectrum of the DFB laser (manufactured by NTT Electronics) when the OEO is in operation. The inset shows the unmodulated spectrum of the semiconductor laser driven by a DC bias current of 50 mA. The simulated optical spectrum and the temporal intensity profile of the DFB laser pulse are presented in the lower panel. (d) In the upper panel is the optical spectrum of the DKS microcomb. The inset shows that the relative intensity difference between the central pumping line and the two first-order PM sidebands is 11.4 dB, corresponding to a PM depth of $\beta \approx 0.5$. The lower panel shows the simulated microcomb spectrum. The inset is the intensity profile of the DKS in the time domain.

II. EXPERIMENTS

To synchronise the repetition frequency of DKSs to an external microwave source whose frequency is close to the microresonator FSR, we phase-modulate the continuous-wave (cw) pump laser at the microwave frequency so the group velocity of the intracavity DKS is locked to the group velocity of the phase gradient potential of the intracavity cw background. As illustrated in Fig. 1 (a), the intracavity DKS is normally trapped at an equilibrium position that is close to the phase maximum of the cw background [10, 11, 25–27]. Yet, the timing jitter contained in the microwave frequency signal, especially those in the relatively short time scales (that are equivalent to phase noises at high frequency offsets) would have damped influence on the motion of the DKS. As a result, the photodetection of the output DKSs can generate a microwave signal whose phase noise at relatively high offset frequencies is much lower than that of the input microwave source, despite that the frequency of the newly generated microwave is unchanged [12, 13].

Figure 1 (b) shows the schematic of the experiment. Laser light with a power of 1 mW produced by a 1546-nm distributed feedback (DFB) laser is coupled into a 9.25-km-long single-mode fiber. The transmitted light is registered by a photodetector (bandwidth ~ 15 GHz), whose voltage output is amplified and then filtered with a custom-made rf bandpass filter (with a center frequency of 14.092 GHz and a 3-dB bandwidth of 25 MHz) before being fed back into the AC level of the bias current of the laser. A variable optical attenuator is manually tuned to adjust the loop gain to obtain a stable OEO signal whose frequency is around the center frequency of the rf bandpass filter. Once the OEO is established, the laser essentially works as a GSL (with an rf modulation power between 15 and 20 dBm), producing periodically modulated waveform that corresponds to a narrow comb in spectrum (see Fig. 1 (c)). We also use laser rate equations to simulate the GSL spectrum and the pulse profile, which are presented in the lower panel of Fig. 1 (c). Details of the simulation can be found in the Supplemental Material [28]. Next, the generated microwave signal is used with an electro-optic modulator (EOM) to add phase modulation (PM) to a 1550-nm external-cavity diode laser (ECDL). The modulated light is then amplified with an erbium-doped fiber amplifier to 300 mW and coupled into a high-Q ($\sim 4 \times 10^8$) resonance in a magnesium fluoride (MgF_2) whispering-gallery-mode microresonator (whose FSR is 14.092 GHz) to generate DKSs [12]. To observe the DKS state, 10% of the transmitted light is sent into

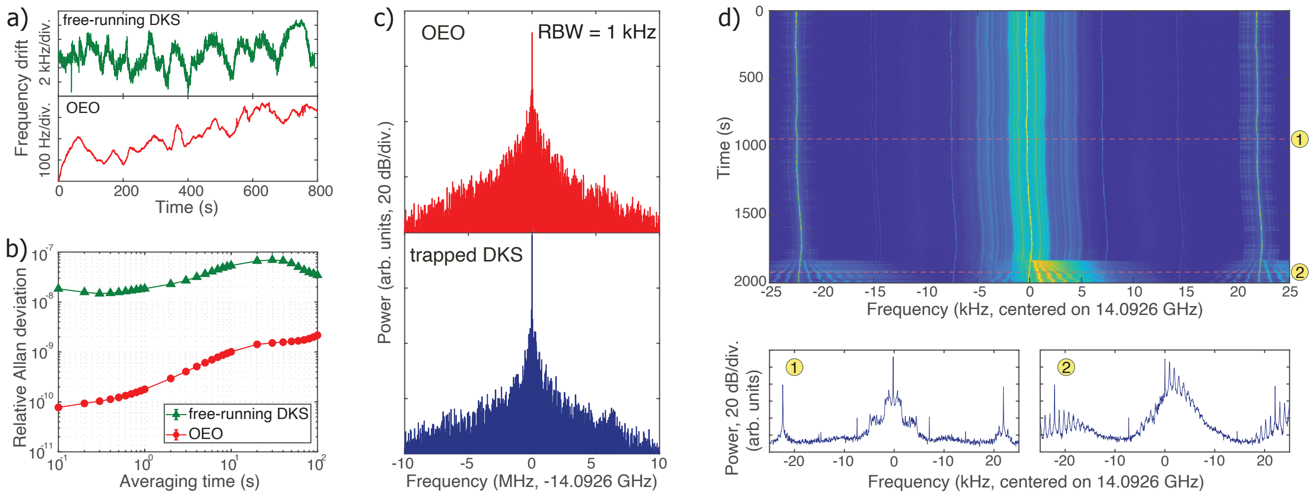

Figure 2. Experimental results of using an OEO to synchronize DKSs. (a) Frequency drifts of the repetition rate of the free-running DKS (upper panel) and the OEO (lower panel). (b) Relative Allan deviations of the frequency instabilities in (a). The error bars are barely visible in the figure due to their small values. (c) The rf spectra of the OEO oscillation signal (upper panel) and the synchronized DKS repetition rate (lower panel). The resolution bandwidth (RBW) of the measurement is 1 kHz. (d) Spectrogram of the DKS repetition rate when the microwave generated by the OEO is used to drive the PM. Two snapshots at the positions denoted by the red dashed lines are displayed in the lower panels, showing the spectral profiles of the synchronized and the unsynchronized DKS repetition rate, respectively.

an optical spectrum analyzer (OSA) for monitoring the microcomb spectrum (see the upper panel in Fig. 1 (d) and the simulated comb spectrum in the lower panel for comparison). The relative intensities of the pump laser and the two first-order PM sidebands indicate that the modulation depth β is nearly 0.5. For the majority (90%) of the transmission, a fiber Bragg grating (FBG)-based optical notch filter is used to filter out the pumping light before the soliton train is detected by a fast photodetector (bandwidth $\sim$ 40 GHz). The rf output port of the photodetector is connected to an electrical spectrum analyzer (ESA) to characterize the spectrum of the DKS repetition rate. Owing to the temperature-stabilized chamber that shelters the microresonator and the self-thermal-stabilization mechanism of the soliton state [29], without any active control on the laser-resonance detuning the DKS state can be maintained for more than an hour. If the PM frequency is close to the intrinsic DKS repetition rate (typically within a mismatch less than a few kHz), only one frequency peak is observed in the rf spectrum of the output solitons, showing that the DKS repetition rate is synchronised to the OEO.

We first compare the frequency stabilities of the OEO and the repetition rate of the free-running DKS (with PM disabled). The measured frequencies are mixed down to approximately 10 MHz and counted by a frequency counter with a gate time of 0.1 s. Figure 2 (a) shows the frequency drifts while the calculated fractional Allan deviations are presented in Fig. 2 (b). Due to the small size of the microresonator and the fluctuation in the uncontrolled laser-resonance detuning, the repetition rate of the free-running DKS exhibits a frequency instability that is higher than that of the OEO by one to two orders of magnitude at averaging times between 0.1 and 100 s. Using a thermistor-heater pair attached to the base of the microresonator setup, we tune the temperature of the microresonator to match the repetition rate of the generated DKS to the OEO frequency. As shown in Fig. 2 (c), soliton trapping is observed as the soliton repetition rate and the OEO frequency are overlapped. Figure 2 (d) presents the spectrogram of the DKS repetition rate recorded in a lapse of 2000 s, showing that the solitons are in a trapped state until the time of $\sim$1840 s. As can be seen from the two spectra taken from the temporal positions denoted by the numbered red dashed lines, when the soliton is trapped, a single intensive peak at the OEO frequency is shown. Adjacent side-modes with a frequency gap of 22.1 kHz are also observed, which is consistent with the estimated FSR of the OEO loop. In contrast, after the soliton trap fails to stably capture the DKS due to the increased mismatch between the OEO frequency and the intrinsic DKS repetition rate, multiple peaks in the spectrum are shown, which is a typical feature of the frequency pulling phenomenon [12].

From Fig. 2 (c) one can already see that the relative intensities of the side-mode oscillations become weaker in the rf spectrum of the trapped DKS repetition rate. In Fig. 3 (a) we further compare the rf spectra of the microwave directly derived from the OEO and that generated by the photodetection of the trapped DKS with a finer RBW of 10 Hz. The amplitude of one of the spectra is offset so the peak powers of the two spectra are aligned to be equal. The comparison clearly shows that the averaged power of the first-order side-mode pair in the DKS spectrum is lower than that in the OEO spectrum by approximately 17 dB, and that a suppression ratio of 25 dB on the second-order side modes is achieved with the trapped DKS. Since the resonance bandwidth of the microresonator is close to 500 kHz that is higher than the OEO FSR by more than one order of magnitude, the strong suppression of the side modes that are within the resonance bandwidth is attributed to the nonlinear spectral filtering effect yielded by the DKS dynamics [12, 13]. Fundamentally, this sub-bandwidth filtering effect is related to the dynamical-attractor nature of DKS, which allows DKS to effectively dissipates external perturbations and to store information longer than the microresonator's photon storage time.

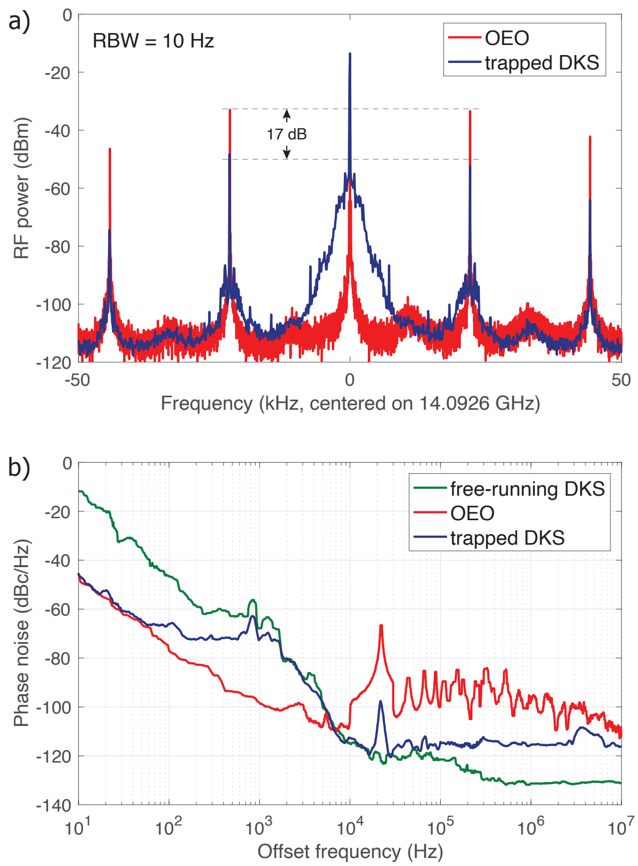

Figure 3. Spectral purification enabled by soliton trapping. (a) Spectra of the OEO oscillation and the repetition rate of the trapped DKS. The DKS spectrum shows suppression ratios of 17 dB for the first-order side modes and 25 dB for the second-order side modes, respectively. (b) Phase noise spectra of the microwave signals. The OEO oscillation signal is tapped from the OEO using a microwave power splitter. The DKS signals are generated by the photodetection of the soliton pulse train with a fast photodetector.

Next, we use a phase noise analyzer (Rohde&Schwarz FSUP26) to acquire the phase noise spectra of the microwave signals. The results are presented in Fig. 3 (b). At offset frequencies below 60 Hz, the phase noise spectrum of the synchronized DKS repetition rate is identical to that of the OEO oscillation, showing that the PM-induced potential gradient tightly locks the soliton repetition rate in this frequency range. Compared with the phase noise of the free-running DKS signal, the phase noise reduction is more than 20 dB at the low offset frequencies, which is in good agreement with the Allan deviation comparison displayed in Fig. 2 (b). Above the offset frequency of 60 Hz, however, the potential gradient starts to lose its full control over the solitons, and the phase noise of the DKS repetition rate becomes closer to that of the free running situation. Owing to the intrinsic ultralow timing jitter of the microresonator DKS [30, 31], this behavior allows the trapped DKS to perform spectral purification on the OEO oscillation. Due to the unsuppressed side modes, the phase noise of the OEO oscillation mainly stays above the level of -100 dBc/Hz at the offset frequencies above 10 kHz. In contrast, in the same offset frequency range the repetition rate of the trapped DKS shows a phase noise magnitude that is decreased by around 20 dB. While the spectral purification effect has been confirmed with the phase noise analysis, we note that the phase noise of the trapped DKS repetition rate is still higher than that of the free running repetition rate by nearly 15 dB at offset frequencies above 300 kHz. It is unexpected because the phase noise reduction effect is supposed to become stronger at higher offset frequencies. We attribute this limitation to the residual pump power of 150 μW contained in the light after the optical notch filter. This residual pump transfers the phase noise spectrum of the OEO into the DKS spectrum via photodetection due to the residual amplitude modulation in the PM process, thus contaminating the spectral purity of the trapped DKS repetition rate. We also observe a rise of the phase noise of the trapped DKS repetition rate around the offset frequency of 4 MHz. This phase noise increase is caused by the DKS relaxation oscillation that has been numerically investigated [32] and experimentally observed in the time domain recently [33].

III. THEORIES AND SIMULATIONS

It has been theoretically derived [25, 27] that when the PM frequency for the cw pump modulation is matched to the natural repetition rate of the DKSs, the drift velocity of a DKS, that is the velocity relative to the co-rotating reference frame, is linearly proportional to the phase gradient ($\phi'(\tau)$) of the intracavity background field as:

$$V_{\mathrm{drift}} \equiv \frac{d\tau}{dt} = \frac{D_2}{D_1^2}\phi'(\tau) \tag{1}$$

where $\tau \in [-\frac{t_{\mathrm{R}}}{2}, \frac{t_{\mathrm{R}}}{2})$ is the temporal position of the DKS in the co-rotating reference frame, t_{R} is the round-trip time, D_1 is the microresonator FSR (in radian), and D_2 is the second-order dispersion coefficient (see [28] for more information on the DKS simulation). With PM applied on the cw pump we write the phase of the intracavity background as $\phi(\tau) = \beta\cos\left(\frac{2\pi\tau}{t_{\mathrm{R}}}\right)$, and the DKS is attracted to the phase maximum at $\tau = 0$. By including the exerted relative displacement $\xi(t)$, the motion of the DKS under the impact of the background phase gradient can be analyzed with:

$$\frac{d\tau}{dt} = -\frac{\beta D_2}{D_1}\sin\left(\frac{2\pi(\tau+\xi(t))}{t_\mathrm{R}}\right) \quad (2)$$

When $\tau+\xi(t)$ is close to 0 (i. e., the amplitude of the timing jitter of the intracavity gradient potential is small), Eq. 2 can be simplified by linearization of the sinusoidal function [13] as:

$$\frac{d\tau}{dt} = -\beta D_2(\tau+\xi(t)) \quad (3)$$

Assuming that $\xi(t)$ is a random process that obeys $\langle\xi(t)\xi(t')\rangle = \epsilon^2\delta(t-t')$, we note that Eq. 3 has the same form of the equation of motion that studies the dynamics of a particle trapped by an optical tweezer in a fluid [34, 35]. Such an equation of motion can be directly solved in the frequency domain by applying Fourier transform, yielding the power spectrum of the DKS motion as:

$$S_{\tau\tau}(\omega) = \frac{\epsilon^2 K^2}{K^2+\omega^2} \quad (4)$$

where $K = \beta D_2$ is the corner frequency. Since normally the modulation depth is of $\beta < 1$, and D_2 is significantly smaller than the loss rate of the microresonator, the DKS-based spectral purification effect is shown at the offset frequencies much lower than the resonance bandwidth. When the magnitude of the power spectrum of $\xi(t)$ is high so the approximation with Eq. 3 is no longer applicable, the motion of the DKS can be numerically computed with arbitrary $\xi(t)$ by using Eq. 2, and one may expect that the noise purification effect becomes weaker as the phase gradient increases with increased deviation of the DKS position from the center of the potential well. Interestingly, as the amplitude of the fluctuation of $\xi(t)$ increases to a certain level that is larger than $\frac{t_\mathrm{R}}{2}$, the noise purification effect can become stronger again because the DKS is completely out of the original trap and the net effect brought by the periodic nature of the potential well is averaged down (see [28] for more information).

Computational models for simulating the OEO dynamics have been developed [36–38], offering a convenient tool to design OEOs and to analyze experimental results. To highlight the potential of using synchronised DKS in OEO side-mode suppression, here we adopt the approach similar to the one in [37] to simulate the microwave phase evolutions of a typical optical-intensity-modulator-based OEO and a GSL-based OEO. Figure 4 (a) plots the diagram of the OEO loop in the simulation. Based on a Mach-Zehnder interferometer intensity modulator (whose modulation response curve that is described by the Bessel function of the first kind [37] is also shown), the OEO loop comprises an rf bandpass filter and a gain section that includes all the gain and loss in the optical-to-electrical and electrical-to-optical conversion processes as well as in the rf amplification and optical transmission. The OEO starts from weak noise, and Gaussian random noise is numerically added to the microwave field envelope in a roundtrip-by-roundtrip fashion. In Fig. 4 (b) and (c) we plot the phase evolution of the microwave field after the OEO is fully built up, showing the period of 2 μs that is in agreement with the round-trip length we set in the simulation. We then use this phase evolution as the phase variation for the DKS-trapping gradient potential to compute the motion of a DKS in an integrated Si_3N_4 microring resonator (FSR = 10 GHz, $Q \sim 10^7$, other parameters can be found in [28]), which allows us to calculate the phase variation of the microwave signal generated by the DKS. Fig. 4 (d) and (e) present the phase evolutions of the DKS-based signal computed with the method based on the Lugiato-Lefever equation (LLE) [12, 39] and the numerical integration of Eq. 2, respectively, showing excellent agreement between these two approaches. Figure 4 (f) shows the phase noise spectra calculated with the data in Fig. 4 (b), (d) and (e). Phase noise spectra of the microwave signal generated by the DKS show significant spectral purification effect with a side-mode suppression ratio of approximately 40 dB for the first-order side mode of the OEO. Comparing the results derived with LLE and the motion equation of Eq. 2 reveals that at offset frequencies above 1.5 MHz the high-order side modes exhibit much higher magnitudes in the LLE-simulation-based spectrum. The reason for this discrepancy is that the LLE method simulates the full soliton dynamics that include the transient soliton profile fluctuations and soliton relaxation oscillations, thus yielding a more accurate phase noise spectrum at the high offset frequency range.

Next, we simulate the GSL-based OEO in our experiment. We simulate the semiconductor laser output pulses with varied bias current modulation amplitudes at the modulation frequency of 14 GHz. Then we calculate the rf spectra of the laser output and obtain the saturable modulation response curve by data fitting (see [28] for more details). As shown in Fig. 4 (g), while the rest of the OEO loop is similar to the one illustrated in Fig. 4 (a), we add an extra loss (i. e., the adjustable loss (AL) in the figure) into the loop to prevent the OEO from oscillating chaotically. This is also in qualitative agreement with our experiment as we need to carefully adjust the variable optical attenuator to secure the stable operation of the OEO. In this simulation the OEO loop length is much longer so the FSR of the OEO is 22.1 kHz – same as the one in our experimental setting. With the rf bandpass filter whose bandwidth is 20 MHz, the small OEO FSR causes intensive side-mode oscillations, which leads to the large phase variations of the OEO signal shown in Fig. 4 (h) and (i). Based on the set of parameters that are in accordance with the MgF_2 microresonators in our experiment, we repeat the DKS noise purification simulation processes using LLE and Eq. 2, respectively. Figure 4 (j) and (k) show the results when the long-term DKS drift is stabilized. We notice that the final trapping point calculated by these two methods differs by ~ 0.16

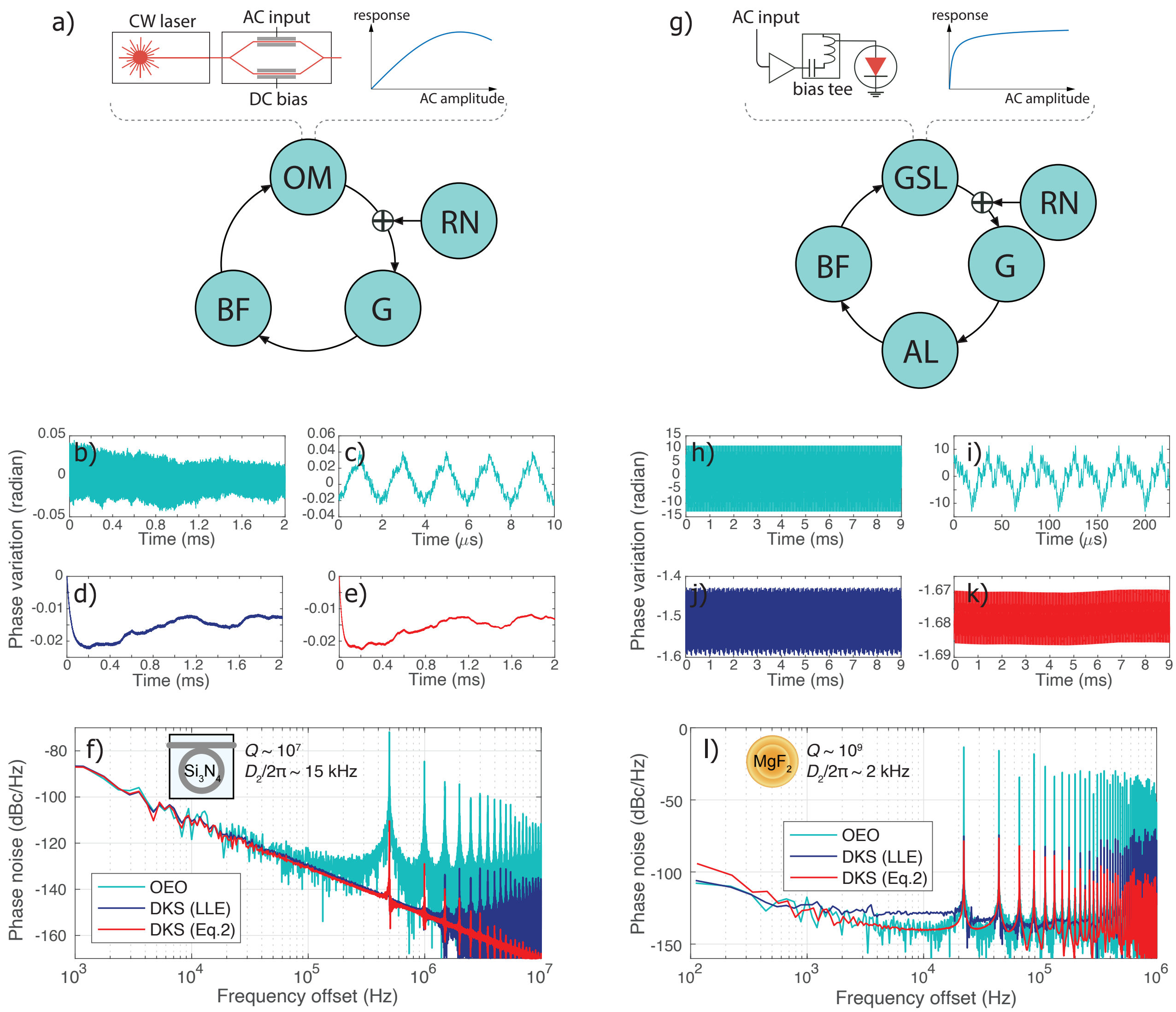

Figure 4. Simulation of synchronized-DKS-based OEO side-mode suppression. (a) Schematic of the computational model of an optical-modulator-based OEO. The Mach-Zehnder interferometer structure of the modulator and the qualitative saturable curve of the modulation response are illustrated. OM: optical modulator; G: gain; BF: bandpass filter; RN: random noise. (b) The simulated phase variation of the 10-GHz OEO signal. (c) A 10-μs-long piece in the curve in (b), showing the details of 5 consecutive round-trips of the phase of the OEO signal. (d, e) Computed phase evolutions of the synchronized DKS when the phase variation in (b) is applied to the intracavity soliton trap. The parameters related to the microresonator are set to be in accordance with an integrated Si_3N_4 microring resonator. The result in (d) is derived with the LLE-based simulation, while the result in (e) is calculated by numerical integration of Eq. 2. (f) Phase noise spectra of the 10-GHz OEO signal and the synchronized-DKS-purified signal computed with the data in (b), (d) and (e), respectively. (g - l) Simulation results similar to (a - f). The modelling of the 14-GHz OEO is based on a GSL and a loop length that is the same as the one in the experiments. An adjustable loss (AL) is included in the loop to mimic the effect of the variable optical attenuator to obtain stable oscillations. For the simulation of the DKS dynamics the microresonator-related parameters are set to be in close agreement with the MgF_2 whispering-gallery-mode resonator used in the experiments.

radian, which may be related to the small parasite amplitude modulation in the intracavity background [10]. Again, computed phase noise spectra in Fig 4 (l) confirm the side-mode suppression phenomenon, showing a suppression ratio of more than 50 dB for the first-order side mode. Such a high suppression ratio may not be easily realized in experiment because the soliton amplitude instability caused by the fluctuation of the phase gradient potential well would be converted into phase noise in the photodetection process, which would set a phase noise floor. Nevertheless, as proved by our experimental results, the synchronized DKS provides a practical approach to effectively filter out the side-mode oscillations in a high-Q OEO.

IV. CONCLUSIONS

In conclusion, an OEO made of a bias-current-modulated semiconductor laser and an optical fiber delay line is developed. Besides the potential in developing cost-effective sources for high-bit-rate optical telecommunications [24] and quantum key distribution [40] based on GSLs, in this work the OEO is implemented to provide a stable microwave signal for trapping microresonator DKS. With the phase gradient cast upon the pumping field, the soliton trap successfully synchronizes the repetition rate of the DKS to the OEO frequency without using any feedback servo control on the pump laser frequency or power. Owing to the low frequency drift of the OEO oscillation, the frequency instability of the DKS repetition rate is suppressed by up to two orders of magnitude. Moreover, the photodetection of the DKS pulse train produces a microwave signal that has the same frequency of the OEO oscillation but with highly suppressed side-mode oscillations because of the nonlinear spectral filtering effect. The hybrid OEO-microcomb system takes advantage of the soliton trapping technique to improve each sub-system's performance with the other party's relative strength, thereby bringing forth an economic solution to versatile optical and microwave metrology. With the recent progress in the miniaturization and integration of both the OEO [41, 42] and the microcomb systems [43, 44], the OEO-microcomb hybridization may be realized in a fully integrated fashion to facilitate the maturation of the portable, energy-efficient, and commercially viable frequency combs.

The data used to produce the plots within this article are available from Zenodo [45].

ACKNOWLEDGMENTS

This publication was supported by Contract No. D18AC00032 (DRINQS) from the Defense Advanced Research Projects Agency (DARPA), Defense Sciences Office (DSO), funding from the Swiss National Science Foundation under grant agreement No. 192293, Science Foundation Ireland (SFI) 15/CDA/3640 and the SFI/European Regional Development Fund (13/RC/2077_P2). This work is also supported by the Air Force Office of Scientific Research under award number FA9550-19-1-0250. W. Weng is the recipient of an Australian Research Council Discovery Early Career Award (project number DE210101904) funded by the Australian Government.

[1] T. J. Kippenberg, A. L. Gaeta, M. Lipson, and M. L. Gorodetsky, Dissipative Kerr solitons in optical microresonators, Science **361**, eaan8083 (2018).

[2] M.-G. Suh, Q.-F. Yang, K. Y. Yang, X. Yi, and K. J. Vahala, Microresonator soliton dual-comb spectroscopy, Science **354**, 600 (2016).

[3] A. Dutt, C. Joshi, X. Ji, J. Cardenas, Y. Okawachi, K. Luke, A. L. Gaeta, and M. Lipson, On-chip dual-comb source for spectroscopy, Science Advances **4**, e1701858 (2018).

[4] J. Riemensberger, A. Lukashchuk, M. Karpov, W. Weng, E. Lucas, J. Liu, and T. J. Kippenberg, Massively parallel coherent laser ranging using a soliton microcomb, Nature **581**, 164 (2020).

[5] Y.-S. Jang, H. Liu, J. Yang, M. Yu, D.-L. Kwong, and C. W. Wong, Nanometric precision distance metrology via hybrid spectrally resolved and homodyne interferometry in a single soliton frequency microcomb, Physical Review Letters **126**, 023903 (2021).

[6] Z. L. Newman, V. Maurice, T. Drake, J. R. Stone, T. C. Briles, D. T. Spencer, C. Fredrick, Q. Li, D. Westly, B. Ilic, *et al.*, Architecture for the photonic integration of an optical atomic clock, Optica **6**, 680 (2019).

[7] J. Feldmann, N. Youngblood, M. Karpov, H. Gehring, X. Li, M. Stappers, M. Le Gallo, X. Fu, A. Lukashchuk, A. S. Raja, *et al.*, Parallel convolutional processing using an integrated photonic tensor core, Nature **589**, 52 (2021).

[8] X. Xu, M. Tan, B. Corcoran, J. Wu, A. Boes, T. G. Nguyen, S. T. Chu, B. E. Little, D. G. Hicks, R. Morandotti, *et al.*, 11 TOPS photonic convolutional accelerator for optical neural networks, Nature **589**, 44 (2021).

[9] E. Obrzud, M. Rainer, A. Harutyunyan, M. H. Anderson, J. Liu, M. Geiselmann, B. Chazelas, S. Kundermann, S. Lecomte, M. Cecconi, A. Ghedina, E. Molinari, F. Pepe, F. Wildi, F. Bouchy, T. J. Kippenberg, and T. Herr, A microphotonic astrocomb, Nature Photonics **13**, 31 (2019).

[10] D. C. Cole, J. R. Stone, M. Erkintalo, K. Y. Yang, X. Yi, K. J. Vahala, and S. B. Papp, Kerr-microresonator solitons from a chirped background, Optica **5**, 1304 (2018).

[11] W. Weng, A. Kaszubowska-Anandarajah, J. He, P. D. Lakshmijayasimha, E. Lucas, J. Liu, P. M. Anandarajah, and T. J. Kippenberg, Gain-switched semiconductor laser driven soliton microcombs, Nature Communications **12**, 1 (2021).

[12] W. Weng, E. Lucas, G. Lihachev, V. Lobanov, H. Guo, M. Gorodetsky, and T. Kippenberg, Spectral purification of microwave signals with disciplined dissipative Kerr solitons, Phys. Rev. Lett. **122**, 013902 (2019).

[13] V. Brasch, E. Obrzud, S. Lecomte, and T. Herr, Nonlinear filtering of an optical pulse train using dissipative Kerr solitons, Optica **6**, 1386 (2019).

[14] M. H. Anderson, R. Bouchand, J. Liu, W. Weng, E. Obrzud, T. Herr, and T. J. Kippenberg, Photonic chip-based resonant supercontinuum via pulse-driven Kerr microresonator solitons, Optica **8**, 771 (2021).

[15] X. S. Yao and L. Maleki, Optoelectronic microwave oscillator, JOSA B **13**, 1725 (1996).

[16] Y. K. Chembo, D. Brunner, M. Jacquot, and L. Larger, Optoelectronic oscillators with time-delayed feedback, Reviews of Modern Physics **91**, 035006 (2019).

[17] T. Bánky, B. Horváth, and T. Berceli, Optimum configuration of multiloop optoelectronic oscillators, JOSA B **23**, 1371 (2006).
[18] K.-H. Lee, J.-Y. Kim, and W.-Y. Choi, A 30-GHz self-injection-locked oscillator having a long optical delay line for phase-noise reduction, IEEE Photonics Technology Letters **19**, 1982 (2007).
[19] E. Shumakher and G. Eisenstein, A novel multiloop optoelectronic oscillator, IEEE Photonics Technology Letters **20**, 1881 (2008).
[20] W. Li and J. Yao, A wideband frequency tunable optoelectronic oscillator incorporating a tunable microwave photonic filter based on phase-modulation to intensity-modulation conversion using a phase-shifted fiber bragg grating, IEEE Transactions on Microwave Theory and Techniques **60**, 1735 (2012).
[21] X. S. Yao and L. Maleki, Multiloop optoelectronic oscillator, IEEE Journal of Quantum Electronics **36**, 79 (2000).
[22] J. Zhang and J. Yao, Parity-time–symmetric optoelectronic oscillator, Science Advances **4**, eaar6782 (2018).
[23] H. Tang, Y. Yu, and X. Zhang, Widely tunable optoelectronic oscillator based on selective parity-time-symmetry breaking, Optica **6**, 944 (2019).
[24] M. Imran, P. M. Anandarajah, A. Kaszubowska-Anandarajah, N. Sambo, and L. Potí, A survey of optical carrier generation techniques for terabit capacity elastic optical networks, IEEE Communications Surveys & Tutorials **20**, 211 (2017).
[25] J. K. Jang, M. Erkintalo, S. Coen, and S. G. Murdoch, Temporal tweezing of light through the trapping and manipulation of temporal cavity solitons, Nature Communications **6**, 7370 (2015).
[26] H. Taheri, A. B. Matsko, and L. Maleki, Optical lattice trap for Kerr solitons, The European Physical Journal D **71**, 153 (2017).
[27] M. Erkintalo, S. G. Murdoch, and S. Coen, Phase and intensity control of dissipative Kerr cavity solitons, Journal of the Royal Society of New Zealand , 1 (2021).
[28] See Supplemental Material at [URL will be inserted by publisher] for more details on simulations of GSL and OEO dynamics.
[29] T. Herr, V. Brasch, J. D. Jost, C. Y. Wang, N. M. Kondratiev, M. L. Gorodetsky, and T. J. Kippenberg, Temporal solitons in optical microresonators, Nature Photonics **8**, 145 (2014).
[30] D. Jeong, D. Kwon, I. Jeon, I. H. Do, J. Kim, and H. Lee, Ultralow jitter silica microcomb, Optica **7**, 1108 (2020).
[31] C. Bao, M.-G. Suh, B. Shen, K. Şafak, A. Dai, H. Wang, L. Wu, Z. Yuan, Q.-F. Yang, A. B. Matsko, *et al.*, Quantum diffusion of microcavity solitons, Nature Physics **17**, 462 (2021).
[32] A. B. Matsko and L. Maleki, Noise conversion in Kerr comb rf photonic oscillators, JOSA B **32**, 232 (2015).
[33] W. Weng, R. Bouchand, and T. J. Kippenberg, Formation and collision of multistability-enabled composite dissipative Kerr solitons, Physical Review X **10**, 021017 (2020).
[34] K. Svoboda and S. M. Block, Biological applications of optical forces, Annual review of biophysics and biomolecular structure **23**, 247 (1994).
[35] K. Berg-Sørensen and H. Flyvbjerg, Power spectrum analysis for optical tweezers, Review of Scientific Instruments **75**, 594 (2004).
[36] Y. K. Chembo, L. Larger, H. Tavernier, R. Bendoula, E. Rubiola, and P. Colet, Dynamic instabilities of microwaves generated with optoelectronic oscillators, Optics Letters **32**, 2571 (2007).
[37] E. C. Levy, M. Horowitz, and C. R. Menyuk, Modeling optoelectronic oscillators, JOSA B **26**, 148 (2009).
[38] E. C. Levy, O. Okusaga, M. Horowitz, C. R. Menyuk, W. Zhou, and G. M. Carter, Comprehensive computational model of single-and dual-loop optoelectronic oscillators with experimental verification, Optics Express **18**, 21461 (2010).
[39] L. Lugiato and R. Lefever, Spatial dissipative structures in passive optical systems, Phys. Rev. Lett. **58**, 2209 (1987).
[40] L. Comandar, M. Lucamarini, B. Fröhlich, J. Dynes, A. Sharpe, S.-B. Tam, Z. Yuan, R. Penty, and A. Shields, Quantum key distribution without detector vulnerabilities using optically seeded lasers, Nature Photonics **10**, 312 (2016).
[41] J. Tang, T. Hao, W. Li, D. Domenech, R. Baños, P. Muñoz, N. Zhu, J. Capmany, and M. Li, Integrated optoelectronic oscillator, Optics Express **26**, 12257 (2018).
[42] W. Zhang and J. Yao, Silicon photonic integrated optoelectronic oscillator for frequency-tunable microwave generation, Journal of Lightwave Technology **36**, 4655 (2018).
[43] B. Shen, L. Chang, J. Liu, H. Wang, Q.-F. Yang, C. Xiang, R. N. Wang, J. He, T. Liu, W. Xie, *et al.*, Integrated turnkey soliton microcombs, Nature **582**, 365 (2020).
[44] C. Xiang, J. Liu, J. Guo, L. Chang, R. N. Wang, W. Weng, J. Peters, W. Xie, Z. Zhang, J. Riemensberger, *et al.*, Laser soliton microcombs heterogeneously integrated on silicon, Science **373**, 99 (2021).
[45] https://doi.org/10.5281/zenodo.5827532.